nature materials

Article

https://doi.org/10.1038/s41563-023-01488-2

A multiscale ion diffusion framework sheds light on the diffusion–stability–hysteresis nexus in metal halide perovskites

Received: 14 December 2021

Accepted: 20 January 2023

Published online: 27 February 2023

Check for updates

Masoud Ghasemi[1,2], Boyu Guo[1], Kasra Darabi[1], Tonghui Wang[1], Kai Wang[3], Chiung-Wei Huang[4], Benjamin M. Lefler[1], Laine Taussig[1], Mihirsinh Chauhan[1], Garrett Baucom[1], Taesoo Kim[1], Enrique D. Gomez[2,3], Joanna M. Atkin[4], Shashank Priya[3] & Aram Amassian[1]

Stability and current–voltage hysteresis stand as major obstacles to the commercialization of metal halide perovskites. Both phenomena have been associated with ion migration, with anecdotal evidence that stable devices yield low hysteresis. However, the underlying mechanisms of the complex stability–hysteresis link remain elusive. Here we present a multiscale diffusion framework that describes vacancy-mediated halide diffusion in polycrystalline metal halide perovskites, differentiating fast grain boundary diffusivity from volume diffusivity that is two to four orders of magnitude slower. Our results reveal an inverse relationship between the activation energies of grain boundary and volume diffusions, such that stable metal halide perovskites exhibiting smaller volume diffusivities are associated with larger grain boundary diffusivities and reduced hysteresis. The elucidation of multiscale halide diffusion in metal halide perovskites reveals complex inner couplings between ion migration in the volume of grains versus grain boundaries, which in turn can predict the stability and hysteresis of metal halide perovskites, providing a clearer path to addressing the outstanding challenges of the field.

Metal halide perovskites (MHPs) have attracted tremendous interest across various areas of solid-state (opto)electronics[1,2] since demonstrating a promising photovoltaic (PV) power conversion efficiency[3–5]. MHPs are soft ionic semiconductors exhibiting extensive ion migration, which has been directly blamed for their degradation and operational anomalies such as hysteresis in optoelectronic devices[6–11]. A growing body of work associates the improved stability of the new generation of MHPs with a reduction of halide ion migration[12,13]. A conundrum then emerges, in that the majority of MHP devices with superior stability simultaneously exhibit reduced hysteretic behaviour[12,14], a phenomenon that has been independently confirmed to require either very fast or cryogenically suppressed halide ion/vacancy transport[11,15,16]. This suggests that different ion migration pathways may be responsible for the degradation and hysteretic behaviours. Existence of multiple diffusion channels makes MHPs analogous to other polycrystalline metals and ionic crystals, where volume and grain boundary (GB) diffusion coefficients differ by three to five orders of magnitude[17–20].

Here, we design an approach for investigating the multiscale diffusion of ions in polycrystalline MHP films. Through this approach, we discover a fundamental link between vacancy-mediated halide

[1]Department of Materials Science and Engineering, and Organic and Carbon Electronics Laboratories (ORaCEL), North Carolina State University, Raleigh, NC, USA. [2]Department of Chemical Engineering, Pennsylvania State University, University Park, PA, USA. [3]Department of Materials Science and Engineering, Pennsylvania State University, University Park, PA, USA. [4]Department of Chemistry, University of North Carolina at Chapel Hill, Chapel Hill, NC, USA. e-mail: mkg5888@psu.edu; aamassi@ncsu.edu

https://doi.org/10.1038/s41563-023-01488-2

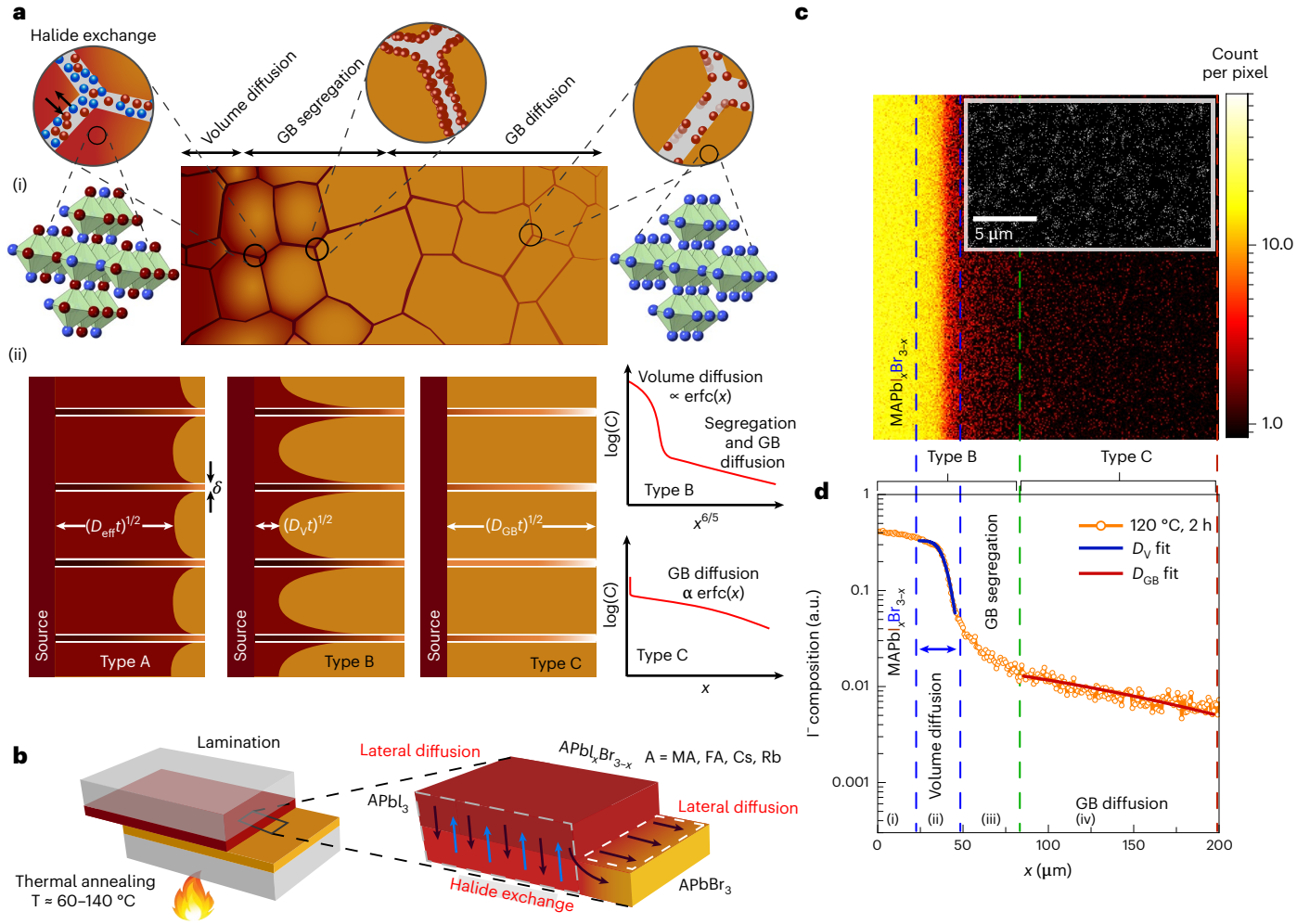

Fig. 1 | Schematic representation of multiscale diffusion in polycrystalline solids, and lateral diffusion profile quantification and modelling. **a**, Schematic of foreign ion diffusion through polycrystalline MHPs with the volume diffusion close to the source, followed by GB segregation and fast diffusion of ions along GBs (i). Schematic of the different types of diffusion and their corresponding diffusion front in polycrystalline MHPs (ii). D_{eff}, D_V and D_{GB} represent the effective diffusion coefficient, volume diffusion coefficient and GB diffusion coefficient, respectively, and t represents diffusion time. The panels on the right show the idealized type B and C diffusion profiles. C and δ represent ion concentration and GB width, respectively. **b**, Schematic of offset laminated samples that are annealed to enable lateral diffusion studies. MA, FA, Cs and Rb represent methylammonium, formamidinium, caesium and rubidium cations, respectively. **c**, The 2D SIMS map of I^- in the host $MAPbBr_3$; the 2D map is collected after annealing of the laminated samples at 120 °C for 2 hours. The dashed lines show the borders of various regions that are labelled in **c** or **d**. The inset shows the 2D SIMS map of the GB diffusion region collected using a PHI nanoTOF II instrument. **d**, The 1D diffusion profile of I^- achieved by integration of the I^- signal in the 2D map over the y axis. The blue and red solid lines show the fit of the erfc function to the volume and GB diffusion regions, respectively, using equations (1) and (2), respectively.

diffusion within the grains and along GBs, which provides a universal relationship between the photostability of MHPs in air and their hysteretic behaviour in devices. The devised approach consists of a lateral diffusion geometry that allows diffusion concentration profiles of foreign halides to be quantified over lateral distances ranging from hundreds of nanometres to hundreds of micrometres within 'thin-film' samples using time-of-flight secondary ion mass spectrometry (ToF-SIMS or SIMS). The quantitative analysis of diffusion profiles reveals two simultaneous channels of ion migration/diffusion: slow diffusion within the bulk or volume of grains and fast diffusion along GBs[21,22]. Analysis of volume and GB diffusion profiles confirms that these occur at drastically different rates and ascribes a difference of two to four orders of magnitude between the volume diffusion coefficient (D_V; ~10^{-14}–10^{-15} $cm^2\ s^{-1}$) and the GB diffusion coefficient (D_{GB}; ~10^{-11}–10^{-10} $cm^2\ s^{-1}$) at room temperature. We find that halides diffuse in the volume of formamidinium (FA)-based MHPs (single and mixed cation) with a D_V that is close to one order of magnitude lower than that of methylammonium (MA)-based MHPs. Additionally, our results show that the activation energy of halide diffusion in the volume (E_V) ranges from 0.61 eV for the bromide ion (Br^-) diffusion in $MAPbI_3$ to a maximum of 0.74 eV for the iodide ion (I^-) diffusion in $FAPbBr_3$, in good agreement with prior reports for halide diffusion activation energy[18]. However, diffusion along GBs takes place with a smaller GB activation energy (E_{GB}; 0.49–0.58 eV)[23,24].

Investigation of halide ion diffusion across archetypal MHPs reveals an inverse relationship between D_{GB} and D_V and their activation energies. The observed small D_{GB} (corresponding to a large E_{GB}) in systems with a large D_V (corresponding to a small E_V), such as $MAPbI_3$, can be attributed to the preference of charged vacancies formed inside the grains to accumulate at GBs[25,26]. Charge balance requirements can cause oppositely charged halide ions to move preferentially in the opposite direction, thus effectively 'weakening' the GB from acting as a barrier for the transfer of fast-moving ions into the volume of grains. These results suggest that 'strong' GBs act as fast ion transport channels and simultaneously allow ions to diffuse along GBs while not 'leaking' easily into the volume of adjacent grains. This relationship provides insight into the stability–diffusion–hysteresis nexus of MHPs

https://doi.org/10.1038/s41563-023-01488-2

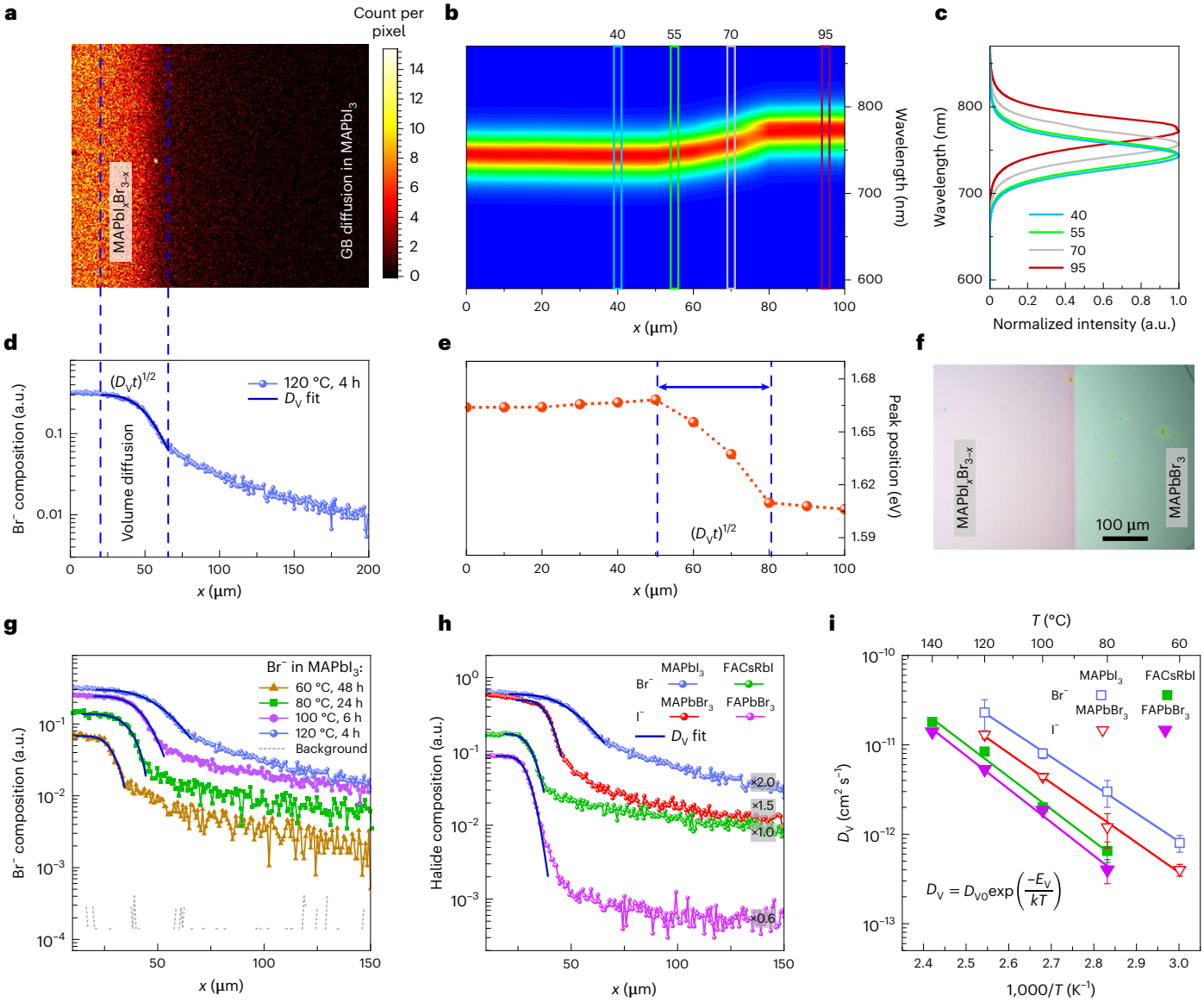

Fig. 2 | Volume diffusion in metal halide perovskites. a,**d** The 2D SIMS map and 1D diffusion profile of Br^- diffusion into $MAPbI_3$ annealed at 120 °C for 4 hours. The dashed blue line shows the volume diffusion fit. **b**, The μPL map of the diffusion front of Br^- diffusion into $MAPbI_3$. **c**, PL spectra from selected positions as shown in **b**. **e**, Emission peak as a function of distance extracted from **b**. The dashed red line serves as a guide to the eye. The dashed blue lines in **d** and **e** show the volume diffusion regions on these profiles. The comparatively smaller volume gradient region's length observed in μPL measurements (<25 μm, marked by the blue arrow) compared to SIMS (>30 μm) can be due to the considerably higher elemental sensitivity of SIMS. **f**, Visible light microscope image of overlap region (purple) and GB diffusion region (green) of I^- diffusion into $MAPbBr_3$. The host $MAPbBr_3$ is used for imaging due to a more clear colour change in bromide samples after the diffusion of I^-. **g**, The 1D SIMS diffusion profiles of Br^- into $MAPbI_3$ at different temperatures. The dashed profile shows the background count, and the blue lines show volume diffusion fits. **h**, Examples of I^- and Br^- diffusion in MHPs with different compositions at 120 °C, including $MAPbX_3$ (X = I, Br), $FAPbBr_3$ and FACsRbI. The concentration profiles are shifted horizontally before fitting to reduce the overlap between profiles. The profiles and their associated volume diffusion fits are also shifted vertically using multiplying factors shown on the plots, for clarity. The blue lines show the volume diffusion fits. **i**, The D_V of halides in MHPs as a function of inverse temperature. Data are presented as the fitted values for D_V extracted from equation (1), ± standard error of the fit. The activation energy and diffusion prefactor are extracted from the slope and intercept of Arrhenius fits (equation shown as inset), respectively. The solid lines show the Arrhenius fits. D_{V0} is the volume diffusion prefactor, E_V is the volume activation energy, k is the Boltzmann constant and T is the absolute temperature.

by directly addressing the observation that the photostability of MHPs in dry air requires a low D_V and is always accompanied by high D_{GB}, thus benefiting from lower hysteresis in devices, as seen predominantly in FA-based compounds[27]. We further demonstrate that traditionally hysteretic materials, such as MA-based systems exhibiting low D_{GB}, can be subjected to successful mitigation strategies such as fullerene passivation[28], in effect strengthening the GBs. To our knowledge, this is the first framework that deconvolutes the volume and GB diffusion of halides in MHPs, leading to the discovery of a coupling between D_V and D_{GB}. This framework takes an important step towards the development of ultrastable MHPs in hysteresis-free devices by prescribing material designs and processing approaches that simultaneously minimize volume diffusion and maximize GB diffusion.

Lateral diffusion geometry and multiscale ion diffusion

Self diffusion and foreign atom diffusion in traditional polycrystalline ceramics and metals, in the absence of surface diffusion, have been shown

https://doi.org/10.1038/s41563-023-01488-2

Table 1 | Summary of volume and GB diffusions in different halide perovskite compositions

Perovskite composition	D_V		D_{GB}		D_V at r.t. ($cm^2 s^{-1}$)[c,d]	D_{GB} at r.t. ($cm^2 s^{-1}$)[c,d]
	D_{V0} ($cm^2 s^{-1}$)[b]	E_V (eV)	D_{GB0} ($cm^2 s^{-1}$)[b]	E_{GB} (eV)		
$MAPbI_3$ (Br^-)[a]	1.8×10^{-3}	0.61±0.02	0.17	0.57±0.03	7×10^{-14}	3×10^{-11}
$MAPbBr_3$ (I^-)	3.8×10^{-3}	0.66±0.03	0.33	0.55±0.02	2×10^{-14}	6×10^{-11}
FACsRbI (Br^-)	1.1×10^{-2}	0.72±0.02	0.07	0.52±0.02	8×10^{-15}	2×10^{-10}
$FAPbBr_3$ (I^-)	1.6×10^{-2}	0.74±0.02	0.03	0.46±0.1	5×10^{-15}	4×10^{-10}

[a]Foreign ion diffusion into the host material. [b]D_{V0} and D_{GB0} are prefactor values extracted from Arrhenius fits ($D = D_0 \exp\left(\frac{-E}{kT}\right)$, where D is the temperature-dependent diffusion coefficient, D_0 is the pre-factor, E is the activation energy, k is the Boltzmann constant, and T is the absolute temperature) to volume and GB diffusion results, respectively. [c]r.t., room temperature. [d]The diffusion coefficients are extracted from an extrapolation of Arrhenius fits.

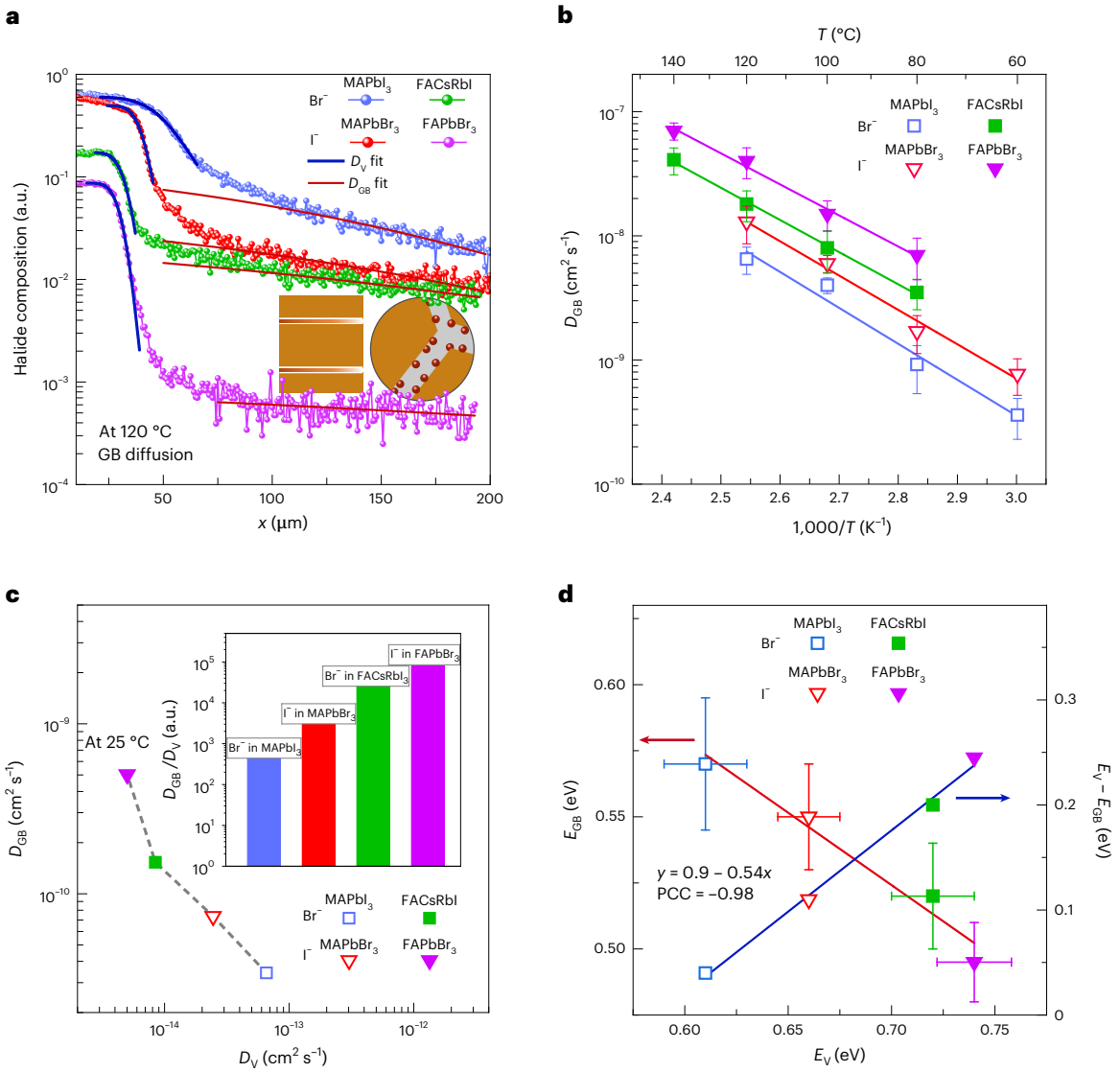

Fig. 3 | GB diffusion as a function of temperature, halide type and composition. a, The 1D SIMS profiles of halide diffusion plotted for different compositions of MHPs collected at 120 °C with the erfc fucntion fit to the diffusion tail. The inset shows the schematic of GB diffusion. **b**, Temperature-dependent D_{GB} in different systems. D_{GB} results are presented as the mean values ± standard deviation of four different fits to GB diffusion profiles. The solid lines show the Arrhenius fits. **c**, The relation between D_{GB} and D_V at 25 °C; the diffusion coefficients are extracted from an extrapolation of Arrhenius fits. The dashed lines are a guide to the eyes. The inset shows the ratio of D_{GB}/D_V at 25 °C for different systems. **d**, GB activation energy (E_{GB}) and the difference between the volume and GB activation energies, plotted against the volume activation energy (E_V); the solid red and blue lines show the linear fits with a Pearson correlation coefficient (PCC) of −0.98 and 0.96, respectively. Data are presented as the E_{GB} and E_V values extracted from the linear fits presented in Fig. 2i and **b**, respectively, ± standard error of the fitted values.

to occur along two primary pathways[20,24,29]: (1) a slower diffusion pathway through the grains of a crystal, which we refer to as volume diffusion; and (2) a fast diffusion pathway along the GBs. The significant differences in the diffusivity of ions through the volume and along GBs mean that polycrystalline samples typically exhibit considerably different diffusion concentration profiles that can be exacerbated by the geometry, temperature

https://doi.org/10.1038/s41563-023-01488-2

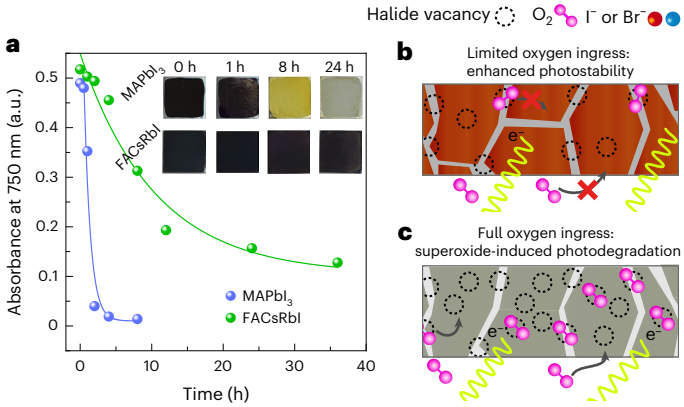

Fig. 4 | Aerobic photodegradation. a, Absorbance at 750 nm for $MAPbI_3$ and FACsRbI as a function of time for samples exposed to dry air and white light (25 mW cm^{-2}) at 60 °C. The inset shows images of different samples at different exposure times. The solid lines are the mono-exponential fit with τ equal to 1.52 ± 0.48 hours and 10.46 ± 2.80 hours for $MAPbI_3$ and FACsRbI, respectively. **b**,**c**, Schematic of superoxide formation in a sample with large D_{GB} and small D_V (**b**) and small D_{GB} and large D_V (**c**). Fast ingress of oxygen into grain interiors through halide vacancy (analogous to a large D_V) causes a higher superoxide formation yield, which in turn leads to a more rapid rate of degradation of the MHP active layer (such as in $MAPbI_3$). Mitigating oxygen ingress in MHPs with smaller halide vacancy densities (such as FACsRbI) reduces the degradation rate. In such systems, oxygen diffusion into grain interiors is considerably slower. e^-, electron.

and duration of diffusion experiments. Based on the Harrison classification, typical concentration profiles observed in polycrystalline metals or ionic crystals can be classified into three main types (types A, B and C)[30]. Among these three diffusion regimes (shown in Fig. 1a and discussed in Supplementary Information), types B and C are the profiles that allow the decoupling of volume and GB diffusions. To the best of our knowledge, types B and C profiles have not been reported in MHPs, and they are not easily created in vertical thin-film stacks due to the high diffusivity of halide ions in MHPs[19,31], which require samples that are tens to hundreds of micrometres thick, making the accurate quantification of D_V and D_{GB} extremely challenging.

Bulk fabrication methods are likely to lose fidelity to solution-processed polycrystalline thin films and, more critically, to make the accurate measurement of concentration depth profiles very challenging. We circumvent these limitations by designing a lateral geometry diffusion experiment (Fig. 1b) that uses polycrystalline MHP thin films identical in preparation and microstructure to ones used in thin-film devices. Importantly, the sample is amenable to lateral imaging and the quantitative analysis of diffusion profiles over multiple length scales (~200 nm to >200 µm) with precision and accuracy. The extended sample geometry has the significant advantage of allowing slow and fast foreign halides to create diffusion concentration profiles at different locations, while the SIMS method can laterally scan these profiles with ease rather than having to perform vertical depth profile measurements that can be subject to measurement artefacts[32].

To perform the lateral geometry diffusion experiments, we laminated pairs of MHP thin films ($MAPbI_3$/$MAPbBr_3$ or $FAPbBr_3$/$FA_{0.85}Cs_{0.1}Rb_{0.05}PbI_3$ referred to hereafter as FACsRbI) with a lateral offset. The top and bottom films exchange halide ions within the overlapping region, but foreign ions are free to diffuse laterally from the contact edge and overlapping region towards the overlap-free region, resulting in the formation of type B and type C concentration profiles of foreign halides over time. Figure 1c,d shows a two-dimensional (2D) SIMS map and integrated one-dimensional (1D) profile, respectively, of I^- lateral diffusion into the $MAPbBr_3$ film after the offset lamination annealing. The I^- diffusion profile shown here extends over hundreds of micrometres and is representative in its extended length to all other diffusion profiles investigated in this report (Supplementary Figs. 1–4). The lateral diffusion profiles are subdivided into four main regions[20,33]. From left to right (as shown in Fig. 1d), these regions are as follows: (i) a flat portion corresponding to the overlap region characterized by halide exchange; (ii) a diffusion gradient region beyond the edge, which marks the start of the lateral diffusion profile (volume diffusion); and (iii, iv) a tail region of the diffusion profiles that exhibits two distinct subregions—region iii, in which the steeper drop in I^- concentration with distance is associated with a region where I^- diffuses and simultaneously accumulates along GBs, also known as GB segregation[20], and region iv, in which the shallower slope in I^- concentration with distance x further from the diffusion edge is associated with diffusion solely along GBs without segregation behaviour (Supplementary Sections 1–5 for more information). The direct diffusion of ions along the GBs is also captured using a PHI nanoTOF II SIMS instrument (inset of Fig. 1c). The combination of our extended lateral sample geometry and the larger GB width reported for MHPs[34], which enables more extensive GB diffusion than in traditional ceramics and metals, is credited for allowing multiscale diffusion to manifest prominently into a hybrid diffusion profile (type B-C).

Quantifying volume diffusion

We first elucidate the volume diffusion properties of foreign halides (I^- and Br^-) across different MHPs through quantitative analysis of type B-C hybrid profiles (Supplementary Figs. 1–4 and Supplementary Information for more information). The complementary error function (erfc) solution of the volume diffusion (equation (1)) can be used to analyse the volume diffusion profile segment of foreign ions:

$$c(x) = c_{V0}\,\mathrm{erfc}\left(\frac{x - x_0}{2\sqrt{D_V t}}\right) \quad (1)$$

where $c(x)$ is the ion concentration at position x, x_0 is the source displacement[31], c_{V0} is the concentration at x_0 and t is the annealing time. Figure 2a,d shows the 2D map and 1D diffusion profiles, respectively, of Br^- in $MAPbI_3$ samples. The diffusion of foreign halides into the lattice of MHP grains causes a bandgap change in the host layer that can be independently probed by optical absorption and emission techniques, such as photoluminescence (PL). We performed micro-PL (µPL) scans across the lateral diffusion edge (Fig. 2b,c,e) to obtain further proof of the volume diffusion of Br^- into $MAPbI_3$ grains. A gradient in emission wavelength extends for ~25 µm from the apparent edge, confirming that the high-concentration region of the erfc profile is dominated by volume diffusion (Supplementary Section 6 for more information). Supplementary Fig. 11 and Fig. 2f show µPL and visible light microscope images, respectively, of the overlap and diffusion regions of I^- diffusion into $MAPbBr_3$. Such a large volume diffusion length through the lattice of MHPs is consistent with the large range of halide diffusivity reported in single-crystal nanowires of caesium lead bromide[31].

Figure 2g,h shows temperature-dependent diffusion profiles of Br^- in $MAPbI_3$ and examples of halide diffusion (I^- or Br^-) in $MAPbBr_3$, $MAPbI_3$, $FAPbBr_3$ and FACsRbI, respectively. Figure 2i summarizes the D_V values with respect to inverse temperature for all the MHP systems investigated. We find that the D_V of halides has an Arrhenius temperature dependence, with the fastest volume diffusion taking place in $MAPbI_3$ (Table 1). The D_V of halides is from six to nearly ten times smaller in FA-based single cation and mixed cation MHPs at all temperatures investigated. In addition, in these systems, the D_V of I^- is smaller than the D_V of Br^-. Importantly, the temperature-dependent analysis across all systems reveals that E_V is the smallest for Br^- diffusion in $MAPbI_3$ (0.61 ± 0.02 eV). On the other hand, the largest E_V was obtained for I^- diffusion in $FAPbBr_3$ (0.74 ± 0.03 eV), with FACsRbI trailing closely behind (0.72 ± 0.02 eV). These variations account for differences in the

https://doi.org/10.1038/s41563-023-01488-2

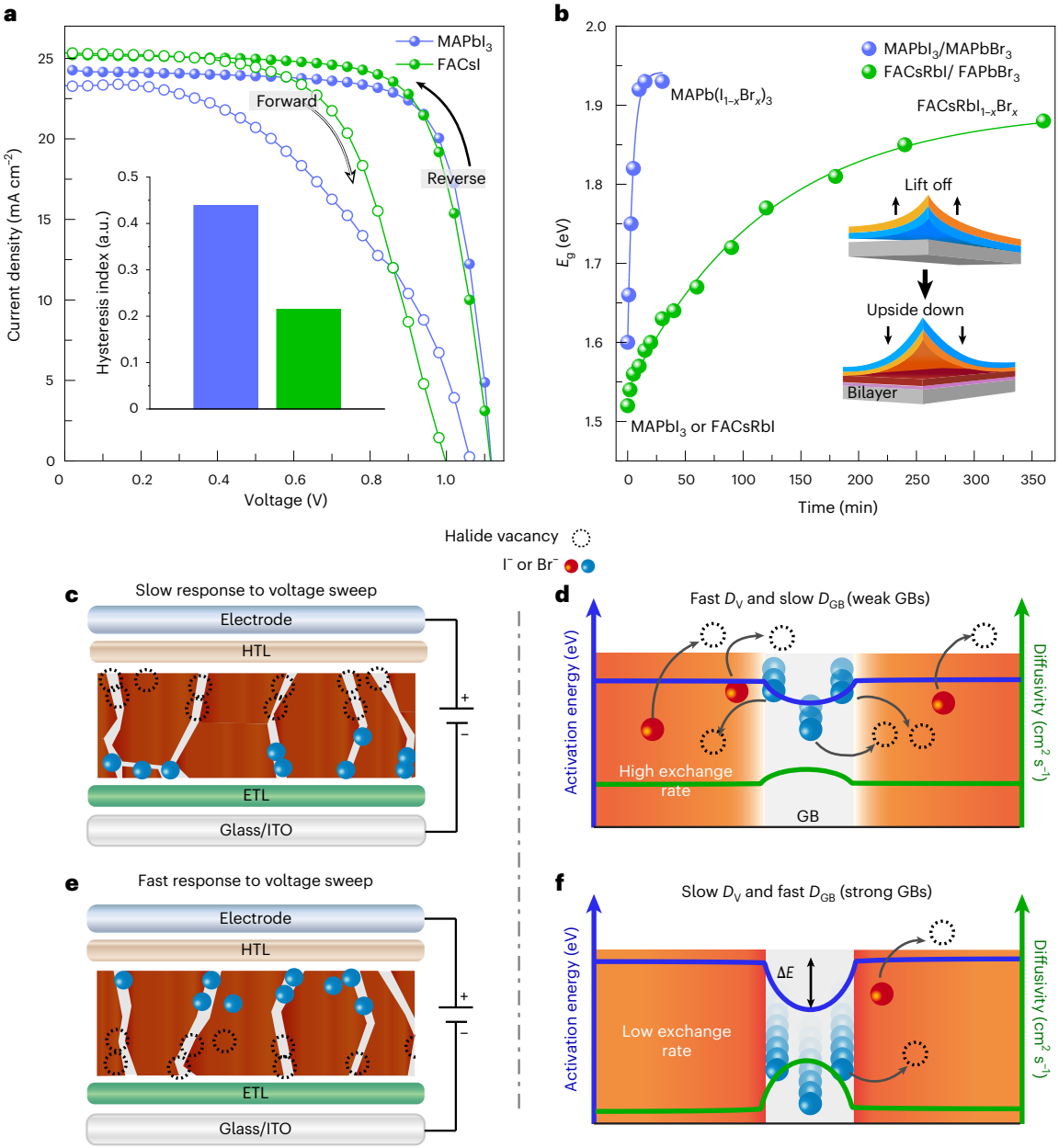

Fig. 5 | Current density versus voltage curves of MHP PVs, halide exchange in MHPs and GB 'strength' model. a, Current density (J) versus voltage (V) curves of $MAPbI_3$ and FACsI perovskite devices under both forward and reverse voltage scans. The inset shows the hysteresis indexes for $MAPbI_3$ and FACsI devices extracted from the forward and reverse scans with a 50 mV s^{-1} scan rate. **b**, The bandgap (E_g) changes in $MAPbI_3/MAPbBr_3$ and FACsRbI/$FAPbBr_3$ heterostructures; the solid lines are a mono-exponential fit with τ equal to 4.7 ± 0.5 minutes and 118.8 ± 9.0 minutes for the $MAPbI_3/MAPbBr_3$ and FACsRbI/$FAPbBr_3$ heterostructures, respectively. The inset in **b** shows the schematic of the lamination process to create a bilayer perovskite structure with intimate contacts (Methods for more information). **c**,**d**, Schematics of halide diffusion along GBs and the D_{GB} relation with J–V hysteresis (**c**) and halide exchange (**d**) in an MHP system with a fast D_V and slow D_{GB} (such as Br^- diffusion into $MAPbI_3$). HTL, ETL and ITO in **c** represent hole transport layer, electron transport layer and indium tin oxide layer, respectively. **e**,**f**, Schematic of halide diffusion along GBs and the D_{GB} relation with J–V hysteresis (**e**) and halide exchange (**f**) in an MHP system with a slow D_V and fast D_{GB} (such as Br^- diffusion into FACsRbI). Higher defect densities in the bulk and GBs of an MHP system such as $MAPbI_3$ lead to a faster diffusion of halide ions from GBs into grain interiors as opposed to diffusion along GBs. This low energy barrier channel (transition from GB to the bulk) in turn reduces D_{GB} and causes a fast halide exchange rate.

diffusion behaviours of I^- and Br^- and greatly favour the diffusivity of halides in MA-based systems over FA-based systems. X-ray photoemission spectroscopy was also used to monitor the lateral distribution of I^- in $FAPbBr_3$ (Supplementary Figs. 14–16). We further validate the proposed volume diffusion framework by investigating the diffusion of I^- into $MAPbBr_3$ single crystals (Supplementary Fig. 18), as detailed in Supplementary Section 8.

A smaller energy barrier for defect formation in MHPs typically enhances volume diffusion by increasing defect concentration[18,35,36]. To elucidate the difference in the density of vacancies in MHP systems, we investigated the rate of superoxide formation using a hydroethidine fluorescent probe[27]. The higher rate of superoxide generation has been correlated with a higher density of vacancies in MHPs[9,27]. As expected, we found that the superoxide yield is lower in FACsRbI compared to $MAPbI_3$ (Supplementary Fig. 20). Our results are consistent with the small formation energy for halide vacancies and interstitials reported for MA-based MHPs compared to their FA-based counterparts[9,37]. We, therefore, associate the larger D_V and smaller E_V values

of halide diffusion in a system such as $MAPbI_3$, compared to FA-based MHPs, with smaller defect formation energies[9,38,39].

Quantifying GB diffusion

We now turn our attention to quantifying the fast motion of ions along GBs. We ascribe a type C regime to the rightmost region of the profile as this is associated solely with the mass transport along the GB (Fig. 3a; Supplementary Information for more information). Equation (2) is employed to fit the tail of the diffusion profile:

$$c(x) = c_{GB0}\,\mathrm{erfc}\left(\frac{x - x_0}{2\sqrt{D_{GB}t}}\right) \quad (2)$$

where c_{GB0} is the ion concentration on grain boundaries. Our analysis of D_{GB} shows an Arrhenius-type behaviour over the temperature range used in this study (Fig. 3b). The fastest foreign halide diffusion along the GB takes place in $FAPbBr_3$, followed by FACsRbI, $MAPbBr_3$ and $MAPbI_3$. The D_{GB} values extrapolated at room temperature are presented in Table 1 and range from 3×10^{-11} to 4×10^{-10} $cm^2\,s^{-1}$.

Fast diffusion of ions has been shown to be one of the main criteria for hysteresis-free PV applications[11,15,40]. Although in most of these cited cases the diffusion coefficients were not directly tied to the GB diffusion, we can see that D_{GB} at room temperature, as determined in our study, is in good agreement with diffusion coefficients reported previously at room temperature: ~10^{-9} to 10^{-11} $cm^2\,s^{-1}$ from transient electrical measurements[15,40]. Nevertheless, the reported transient-measurement-based diffusion quantities in the literature are driven by the net mass transport of ions in the presence of an external electrical field[41]. However, the diffusion coefficient through the volume of grains, that is, three to five orders of magnitude smaller compared to GBs ($D_{GB} \gg D_V$), can explain why ion transport in transient electrical measurements should be GB dominated.

A non-trivial and meaningful inverse relationship emerges when we plot room temperature D_{GB} versus D_V (Fig. 3c) across different MHP systems. This relationship translates to a linear relationship between their respective activation energies (E_V versus E_{GB}; Fig. 3d). From these relationships, it emerges that the fastest volume diffusion (smallest E_V) and slowest GB diffusion (smallest D_{GB} and largest E_{GB}) of all MHPs investigated belong to the same system: $MAPbI_3$. By contrast, the slowest volume diffusion (largest E_V) and fastest GB diffusion (smallest E_{GB}) belong to $FAPbBr_3$.

Linking multiscale diffusion to stability and hysteresis

Due to the role of halide vacancies as reaction mediators for superoxide formation and the subsequent photodegradation of MHPs, the light-induced degradation rate in oxygen can be used as an indirect proxy for halide diffusion[27]. We characterized the oxygen-induced photodegradation of different MHP thin films and corresponding PVs. As Fig. 4a and Supplementary Fig. 22 show, $MAPbI_3$ (D_V at 60 °C = 8.4×10^{-13} $cm^2\,s^{-1}$) degrades very quickly (τ = 1.52 hours, where τ is the degradation time constant) in the presence of light and dry air, while FACsRbI (D_V at 60 °C = 1.5×10^{-13} $cm^2\,s^{-1}$) degrades at a slower rate (τ = 10.46 hours) and partly maintains its dark perovskite phase after light exposure at 60 °C for over 24 hours. A close correlation between D_V and the degradation rate becomes more apparent when we compare the ratio of the degradation time constants at 60 °C (10.46/1.52) with the inverse ratio of D_V values ($8.4 \times 10^{-13}/1.5 \times 10^{-13}$) at this temperature, 5.6 versus 6.9, respectively. A similar trend is observed in the operational stability of unencapsulated PVs under maximum power point tracking conditions (Supplementary Fig. 23), with $MAPbI_3$ showing a faster degradation rate than the FA-based mixed cation system. The larger grain size of $MAPbI_3$ compared to FACsRbI samples (Supplementary Fig. 24) observed in scanning electron microscopy images also rules out the effect of grain size in the faster degradation of $MAPbI_3$ (ref. [42]).

The faster degradation of $MAPbI_3$ is attributed to the larger vacancy density in this system, which facilitates diffusion of halide ions and oxygen and therefore mediates the rate of formation of superoxide species in the bulk of MHP[9,27]. Figure 4b,c shows the schematics of MHPs with fast D_V (high degradation rate) and slow D_V (low degradation rate). We should emphasize that grain heterogeneity and intragrain defects can also play a role in volume diffusion properties. Identifying the correlation between intragrain structures with volume and GB diffusions calls for detailed nanoscale studies in the future[43–45].

While a lower D_V in FA-based systems explains their improved photostability, the difference of nearly one order of magnitude in D_{GB} at room temperature between MA-based and FA-based systems also explains the reduction in hysteretic behaviour of FA-based devices compared to MA-based MHPs[15,40]. A smaller hysteresis index calculated for the mixed-cation-based PVs on forward and reverse voltage scans, compared to $MAPbI_3$, also attests to a larger D_{GB} of ions in FA-based systems (Fig. 5a). Our results show that the hysteresis index can be further reduced by preparing PV devices based on a mixed halide composition (Supplementary Figs. 25 and 26 and Supplementary Tables 2–4)[9]. Additionally, based on the inverse relation between D_{GB} and D_V, and the larger size of I^-, which leads to a slower D_V of these species, we hypothesize that iodide ions/vacancies should be the fastest ionic species moving along the GBs of mixed halide MHPs. To confirm our hypothesis, we designed a double-halide diffusion experiment in which a mixed halide system, $FA_{0.85}Cs_{0.15}Pb(I_{0.95}Cl_{0.05})_3$, is brought in contact with the host $FAPbBr_3$. As Supplementary Fig. 27 shows, Cl^- diffuses with an ~25 times faster diffusion rate compared to I^- into the volume of $FAPbBr_3$. Meanwhile, along the GBs, Cl^- ions diffuse ~4 times slower compared to I^-. These results, including the coupling and inverse relationship between D_V and D_{GB}, highlight that it is the suppression of ion migration into the interior of grains that promotes faster ion diffusion along the GBs.

Employing molecules such as phenyl-C61-butyric acid methyl ester (PCBM) and large cations such as phenethylammonium (PEA^+) as GB-passivating agents has been reported to lead to hysteresis reduction[28,46]. To elucidate the effect of GB passivation, we introduced PEAI and PCBM passivation into $MAPbI_3$ thin-film sample preparation (Supplementary Figs. 28 and 29). As can be seen, both PCBM and PEAI passivation approaches lead to an increase in D_{GB} and a decrease in D_V in passivated samples compared to a control of $MAPbI_3$. This result is also consistent with the reported superior environmental stability of passivated samples and the slight increase in light stability observed here for $MAPbI_3$ (refs. [28,47,48]). The combination of larger D_{GB} and smaller D_V in passivated samples indicates that mitigation approaches successfully improve the hysteretic behaviour by acting upon both GB and volume diffusion processes simultaneously but in opposing ways.

We further use the well-established axial interdiffusion geometry (two compositionally distinct MHPs sandwiched together) to develop a simple prescreening approach for photostability and hysteresis (Methods for more information and Supplementary Figs. 30–32)[17,49]. In Fig. 5b, we observe a much faster homogenization time (5 min versus 118 min) in $MAPbI_3/MAPbBr_3$ bilayers (large D_V) compared to FACsRbI/$FAPbBr_3$ (small D_V). This ~24-times-slower homogenization time demonstrates that halide exchange is rate limited by volume diffusion rather than GB diffusion. This simple method can therefore help predict the photostability of polycrystalline MHPs in relation to MA-based and FA-based MHPs. Conversely, materials that undergo rapid homogenization are predicted to exhibit hysteretic behaviour in devices owing to the inverse link between large D_V and low D_{GB}.

GB 'strength' model

We propose viewing the difference between E_V and E_{GB} (ΔE) as a measure of the similarity in barriers to halide diffusion exerted within grains versus at GBs, with consequences for hysteresis and photostability. A smaller ΔE is synonymous with 'weaker' GBs (Fig. 5c,d) that more easily allow halide exchange between the grain and its boundaries.

By contrast, 'stronger' GBs promote halide motion preferentially along the GBs as opposed to halides occupying vacancy sites within grains (Fig. 5e,f). We find that ΔE (Fig. 3d) is the largest for FA-based systems and approaches zero for $MAPbI_3$. This result indicates that both the volume and GBs exert similar barriers to ion diffusion in $MAPbI_3$. We argue that a reduction in E_V (for example, in $MAPbI_3$), in combination with the preference of positively charged vacancies to accumulate at GBs[25,26,50], can cause the 'weakening' of GBs ($\Delta E \rightarrow 0$). We thus attribute the inverse relation between E_V and E_{GB} and, in particular, the reduction of ΔE from 0.25 eV for FA-based systems to <0.05 eV for $MAPbI_3$, to the loss of a preference for ion motion along GB vacancies and to the facile motion through the volume of grains.

A large halide vacancy concentration in MHPs also acts as a pathway for oxygen diffusion and a catalyst for superoxide formation in the presence of light, which causes a faster photodegradation rate in MHPs exhibiting larger D_V and weak GBs[27]. The combination of fast volume and slow GB diffusions in $MAPbI_3$ explains the vexing properties of conventionally processed $MAPbI_3$ of exhibiting hysteretic behaviour in devices[48,51], rapid photo-induced halide segregation[52,53] in $MAPbI_{3-x}Br_x$ and fast photodegradation in air. By contrast, FA-based systems exhibit the strongest GBs, which create an energy barrier against halide exchange between the GB and the volume of the grains with the benefit of reducing the rate of photodegradation by limiting oxygen ingress in the volume. The strong GBs are characterized by a very large contrast in diffusivity ($D_{GB}/D_V \approx 10^4$–10^5) that favours a reduced hysteresis[14]. The deconvolution of fast GB and slow volume diffusion pathways in polycrystalline MHPs and the direct evaluation of volume diffusion in $MAPbBr_3$ single crystals in our work should put to rest the ongoing debate on the role of GBs in the diffusion properties of MHPs[25,54].

Outlook

Halide ions/vacancies and their subsequent migration in polycrystalline MHPs have been shown to be the most consequential ion migration in MHPs. Nevertheless, a detailed understanding of halide ion migration in polycrystalline MHPs remained inaccessible. The direct observation of multiscale halide ion diffusion presented in this work associates fast-moving ions in devices with ions diffusing along GBs, while phenomena such as the light-induced degradation of MHPs can be quantitatively described by the slow vacancy-mediated diffusion of halide ions and oxygen through the volume of the grains. Our results show that small volume and large GB diffusivities are a necessary combination for achieving stable and hysteresis-free MHP devices, requiring strong GBs that confine fast ion motion to the GB. The GB strength model shows how material composition and passivation methods work and provides a guideline for designing strong GBs towards the development of ultrastable and hysteresis-free MHP devices. The multiscale diffusion framework will also contribute to elaborating accurate models of ion migration in MHPs across a wide range of scenarios, including devices under external stresses and across different applications.

Online content

Any methods, additional references, Nature Portfolio reporting summaries, source data, extended data, supplementary information, acknowledgements, peer review information; details of author contributions and competing interests; and statements of data and code availability are available at https://doi.org/10.1038/s41563-023-01488-2.

References

1. Tan, Z.-K. et al. Bright light-emitting diodes based on organometal halide perovskite. *Nat. Nanotechnol.* **9**, 687–692 (2014).
2. Fang, Y. et al. Highly narrowband perovskite single-crystal photodetectors enabled by surface-charge recombination. *Nat. Photon.* **9**, 679–686 (2015).
3. Burschka, J. et al. Sequential deposition as a route to high-performance perovskite-sensitized solar cells. *Nature* **499**, 316–319 (2013).
4. Kojima, A., Teshima, K., Shirai, Y. & Miyasaka, T. Organometal halide perovskites as visible-light sensitizers for photovoltaic cells. *J. Am. Chem. Soc.* **131**, 6050–6051 (2009).
5. Lee, M. M. et al. Efficient hybrid solar cells based on meso-superstructured organometal halide perovskites. *Science* **338**, 643–647 (2012).
6. Li, Z. et al. Extrinsic ion migration in perovskite solar cells. *Energy Environ. Sci.* **10**, 1234–1242 (2017).
7. Hassan, Y. et al. Ligand-engineered bandgap stability in mixed-halide perovskite LEDs. *Nature* **591**, 72–77 (2021).
8. Mao, W. et al. Light-induced reversal of ion segregation in mixed-halide perovskites. *Nat. Mater.* **20**, 55–61 (2021).
9. Saidaminov, M. I. et al. Suppression of atomic vacancies via incorporation of isovalent small ions to increase the stability of halide perovskite solar cells in ambient air. *Nat. Energy* **3**, 648–654 (2018).
10. Maiti, A., Chatterjee, S., Peedikakkandy, L. & Pal, A. J. Defects and their passivation in hybrid halide perovskites toward solar cell applications. *Sol. RRL* **4**, 2000505 (2020).
11. Richardson, G. et al. Can slow-moving ions explain hysteresis in the current–voltage curves of perovskite solar cells? *Energy Environ. Sci.* **9**, 1476–1485 (2016).
12. Bai, S. et al. Planar perovskite solar cells with long-term stability using ionic liquid additives. *Nature* **571**, 245–250 (2019).
13. Zhao, Y. et al. Suppressing ion migration in metal halide perovskite via interstitial doping with a trace amount of multivalent cations. *Nat. Mater.* **21**, 1396–1402 (2022).
14. Turren-Cruz, S.-H., Hagfeldt, A. & Saliba, M. Methylammonium-free, high-performance, and stable perovskite solar cells on a planar architecture. *Science* **362**, 449–453 (2018).
15. Bertoluzzi, L. et al. In situ measurement of electric-field screening in hysteresis-free PTAA/$FA_{0.83}Cs_{0.17}Pb(I_{0.83}Br_{0.17})_3$/C60 perovskite solar cells gives an ion mobility of $\sim 3\times10^{-7}\,cm^2/(V\,s)$, 2 orders of magnitude faster than reported for metal-oxide-contacted perovskite cells with hysteresis. *J. Am. Chem. Soc.* **140**, 12775–12784 (2018).
16. Zhang, C. et al. Temperature-dependent electric field poling effects in $CH_3NH_3PbI_3$ optoelectronic devices. *J. Phys. Chem. Lett.* **8**, 1429–1435 (2017).
17. Elmelund, T., Scheidt, R. A., Seger, B. & Kamat, P. V. Bidirectional halide ion exchange in paired lead halide perovskite films with thermal activation. *ACS Energy Lett.* **4**, 1961–1969 (2019).
18. Eames, C. et al. Ionic transport in hybrid lead iodide perovskite solar cells. *Nat. Commun.* **6**, 7497 (2015).
19. Sajedi Alvar, M., Blom, P. W. M. & Wetzelaer, G.-J. A. H. Space-charge-limited electron and hole currents in hybrid organic-inorganic perovskites. *Nat. Commun.* **11**, 4023 (2020).
20. Mehrer, H. *Diffusion in Solids: Fundamentals, Methods, Materials, Diffusion-Controlled Processes* Vol. 155 (Springer, 2007).
21. Suzuoka, T. Lattice and grain boundary diffusion in polycrystals. *Trans. Jpn Inst. Met.* **2**, 25–32 (1961).
22. Mishin, Y. M. in *Defect and Diffusion Forum* Vol. 194 1113–1126 (Trans Tech Publications, 2001).
23. Joesten, R. in *Diffusion, Atomic Ordering, and Mass Transport: Selected Topics in Geochemistry* (ed. Ganguly, J.) 345–395 (Springer, 1991).
24. Laemmle, A. et al. Investigation of the diffusion behavior of sodium in $Cu(In,Ga)Se_2$ layers. *J. Appl. Phys.* **115**, 154501 (2014).
25. Phung, N. et al. The role of grain boundaries on ionic defect migration in metal halide perovskites. *Adv. Energy Mater.* **10**, 1903735 (2020).

26. Park, J.-S. et al. Accumulation of deep traps at grain boundaries in halide perovskites. *ACS Energy Lett.* **4**, 1321–1327 (2019).
27. Aristidou, N. et al. Fast oxygen diffusion and iodide defects mediate oxygen-induced degradation of perovskite solar cells. *Nat. Commun.* **8**, 15218 (2017).
28. Shao, Y. et al. Origin and elimination of photocurrent hysteresis by fullerene passivation in $CH_3NH_3PbI_3$ planar heterojunction solar cells. *Nat. Commun.* **5**, 5784 (2014).
29. Kowalski, K., Bernasik, A. & Sadowski, A. Bulk and grain boundary diffusion of titanium in yttria-stabilized zirconia. *J. Eur. Ceram. Soc.* **20**, 951–958 (2000).
30. Harrison, L. Influence of dislocations on diffusion kinetics in solids with particular reference to the alkali halides. *J. Chem. Soc. Faraday Trans.* **57**, 1191–1199 (1961).
31. Pan, D. et al. Visualization and studies of ion-diffusion kinetics in cesium lead bromide perovskite nanowires. *Nano Lett.* **18**, 1807–1813 (2018).
32. Harvey, S. P. et al. Mitigating measurement artifacts in TOF-SIMS analysis of perovskite solar cells. *ACS Appl. Mater. Interfaces* **11**, 30911–30918 (2019).
33. Vaidya, M. et al. Ni tracer diffusion in CoCrFeNi and CoCrFeMnNi high entropy alloys. *J. Alloy. Compd.* **688**, 994–1001 (2016).
34. Shao, Y. et al. Grain boundary dominated ion migration in polycrystalline organic–inorganic halide perovskite films. *Energy Environ. Sci.* **9**, 1752–1759 (2016).
35. Azpiroz, J. M., Mosconi, E., Bisquert, J. & De Angelis, F. Defect migration in methylammonium lead iodide and its role in perovskite solar cell operation. *Energy Environ. Sci.* **8**, 2118–2127 (2015).
36. Delugas, P., Caddeo, C., Filippetti, A. & Mattoni, A. Thermally activated point defect diffusion in methylammonium lead trihalide: anisotropic and ultrahigh mobility of iodine. *J. Phys. Chem. Lett.* **7**, 2356–2361 (2016).
37. Oranskaia, A. et al. Halogen migration in hybrid perovskites: the organic cation matters. *J. Phys. Chem. Lett.* **9**, 5474–5480 (2018).
38. Walsh, A. et al. Self-regulation mechanism for charged point defects in hybrid halide perovskites. *Angew. Chem. Int. Ed.* **54**, 1791–1794 (2015).
39. Alarousu, E. et al. Ultralong radiative states in hybrid perovskite crystals: compositions for submillimeter diffusion lengths. *J. Phys. Chem. Lett.* **8**, 4386–4390 (2017).
40. Sajedi Alvar, M., Blom, P. W. M. & Wetzelaer, G.-J. A. H. Device model for methylammonium lead iodide perovskite with experimentally validated ion dynamics. *Adv. Electron. Mater.* **6**, 1900935 (2020).
41. Lee, J.-W. et al. The role of grain boundaries in perovskite solar cells. *Mater. Today Energy* **7**, 149–160 (2018).
42. Cao, Q. et al. Efficient and stable inverted perovskite solar cells with very high fill factors via incorporation of star-shaped polymer. *Sci. Adv.* **7**, eabg0633 (2021).
43. Tennyson, E. M., Doherty, T. A. S. & Stranks, S. D. Heterogeneity at multiple length scales in halide perovskite semiconductors. *Nat. Rev. Mater.* **4**, 573–587 (2019).
44. Jariwala, S. et al. Local crystal misorientation influences non-radiative recombination in halide perovskites. *Joule* **3**, 3048–3060 (2019).
45. Li, W. et al. The critical role of composition-dependent intragrain planar defects in the performance of $MA_{1-x}FA_xPbI_3$ perovskite solar cells. *Nat. Energy* **6**, 624–632 (2021).
46. Lee, D. S. et al. Passivation of grain boundaries by phenethylammonium in formamidinium-methylammonium lead halide perovskite solar cells. *ACS Energy Lett.* **3**, 647–654 (2018).
47. Wang, H. et al. Interfacial residual stress relaxation in perovskite solar cells with improved stability. *Adv. Mater.* **31**, 1904408 (2019).
48. Niu, T. et al. Stable high-performance perovskite solar cells via grain boundary passivation. *Adv. Mater.* **30**, 1706576 (2018).
49. Akriti et al. Layer-by-layer anionic diffusion in two-dimensional halide perovskite vertical heterostructures. *Nat. Nanotechnol.* **16**, 584–591 (2021).
50. Yun, J. S. et al. Critical role of grain boundaries for ion migration in formamidinium and methylammonium lead halide perovskite solar cells. *Adv. Energy Mater.* **6**, 1600330 (2016).
51. Gao, X.-X. et al. Stable and high-efficiency methylammonium-free perovskite solar cells. *Adv. Mater.* **32**, 1905502 (2020).
52. Kuno, M. & Brennan, M. C. What exactly causes light-induced halide segregation in mixed-halide perovskites? *Matter* **2**, 21–23 (2020).
53. Hoke, E. T. et al. Reversible photo-induced trap formation in mixed-halide hybrid perovskites for photovoltaics. *Chem. Sci.* **6**, 613–617 (2015).
54. McGovern, L. et al. Grain size influences activation energy and migration pathways in $MAPbBr_3$ perovskite solar cells. *J. Phys. Chem. Lett.* **12**, 2423–2428 (2021).

Methods

Materials

MA iodide (MAI, 99.99%), MA bromide (MABr, 99.99%), FA iodide (FAI, 99.99%), FA bromide (FABr, 99.99%) and TiO_2 paste (Dyesol 18NR-T) were purchased from Greatcell Energy. The lead bromide ($PbBr_2$, 99.999%) and lead iodide (PbI_2, 99.999%) used for all thin-film processing except for the device fabrication that took place at Penn State University were purchased from TCI. The lead iodide (PbI_2, 99.99%) and lead bromide ($PbBr_2$, 99.99%) used for device fabrication were purchased from Acros Organics. The tin oxide (SnO_2) non-particle dispersion in water with a concentration of 15 mg ml^{-1} was purchased from Alfa Asar. The solution was diluted to 3 mg ml^{-1} using deionized water prior to coating. PEAI (98%), caesium iodide (CsI, 99.9%), rubidium iodide (RbI, 99.9%), titanium(IV) isopropoxide (99.999%), bis(trifluoromethane)-sulfonimide lithium salt (99.95%), methylammonium solution (ethanol-MA; 33% in absolute ethanol), acetone, acetonitrile, chlorobenzene (CB), 4-*tert*-butylpyridine, rubidium iodide (RbI, 99.9%), caesium iodide (CsI, 99.9%), dimethylformamide (DMF) and dimethyl sulfoxide (DMSO) were purchased from Sigma-Aldrich. The 2,2′,7,7′-tetrakis(*N*,*N*-di(4-methoxyphenyl)amino)-9,9′-spirobifluorene (spiro-OMeTAD) was purchased from Lumtec Corp. Fluorine-doped tin oxide (FTO) glass (8 ohms square (Ω sq^{-1})) was purchased from Wuhan Jingge Technology. All the chemicals were used as received without any further purification.

Preparation of SIMS samples

$FA_{0.8}Cs_{0.15}Rb_{0.05}PbI_3$, $MAPbI_3$, $FAPbBr_3$ and $MAPbBr_3$ perovskite solutions were prepared using mixed solvents of DMF and DMSO with a 4:1 v/v ratio. The iodide and bromide perovskite solutions were prepared by dissolving 1.2 M and 0.8 M, respectively, slate components in the mixed solvents. All solutions were prepared in a nitrogen-filled glove box and were stirred for at least 4 hours at room temperature. The precursor solution was spin-coated on a precleaned SiO_2/Si substrate. The SiO_2/Si wafers with 500 nm thermal oxide were purchased from University Wafers. The substrate cleaning process consists of subsequent water plus detergent, water, acetone and isopropyl alcohol sonication steps, each for 20 minutes. The cleaned substrates then were exposed to UV–ozone for 30 min prior to spin-coating of the perovskite precursor. All films were spin-coated through a one-step spin-coating process with the dripping of CB as an anti-solvent at different times for different perovskite precursors. The $FA_{0.8}Cs_{0.15}Rb_{0.05}PbI_3$ precursor was spin-coated at 5,000 r.p.m. for 30 seconds with a 300 µl drip of CB taking place 18 seconds into the spin-coating. The coated $FA_{0.8}Cs_{0.15}Rb_{0.05}PbI_3$ was quickly moved to a preheated hotplate at 100 °C and baked for 30 minutes. The $MAPbI_3$ precursor was spin-coated at 5,000 r.p.m. for 30 s with a 400 µl drip of CB taking place continuously for 5 seconds, starting at 108–1,211 seconds into the spin-coating and ending at ~16 seconds before the end of the spin-coating step. The coated $MAPbI_3$ was quickly moved to a preheated hotplate at 100 °C and baked for 20 minutes. The $FAPbBr_3$ precursor was spin-coated at 4,000 r.p.m. for 25 seconds with a 300 µl drip of CB taking place 16 seconds into the spin-coating. The coated $FAPbBr_3$ was quickly moved to a preheated hotplate at 150 °C and baked for 30 minutes. The $MAPbBr_3$ precursor was spin-coated at 4,000 r.p.m. for 25 seconds with a 300 µl drip of CB taking place 12 seconds into the spin-coating. The coated $MAPbBr_3$ was quickly moved to a preheated hotplate at 100 °C and baked for 20 minutes.

To avoid the edge area of the perovskite films, the substrates were cleaved using a diamond cutter. The cleaved substrates then were carefully placed on top of each other and held with binder clips to create offset laminated samples for SIMS measurements. The laminated samples then were moved to a nitrogen-filled preheated oven to be baked at different temperatures and for different time durations. The temperature of the oven was measured using a National Institute of Standards and Technology calibrated thermometer. At the end of an annealing step, the binder clips were quickly removed, and the substrates were placed on a large aluminium plate kept at room temperature.

Single-crystal fabrication and polishing

The $MAPbBr_3$ single crystal was grown via the inverse temperature crystallization method. Some 1 M $MAPbBr_3$ precursor solution was prepared in DMF and filtered with a 0.2 µm polytetrafluoroethylene filter before use. The precursor was then heated at 78 °C in an oil bath without any disturbance for 8–12 hours until the single crystal reached the ideal size (~5 mm). The as-grown single crystals were collected and washed in cyclohexane (anhydrous, 99.5%, Sigma-Aldrich) for 10 minutes to remove the residue solution, followed by drying in the vacuum oven at 60 °C overnight. For the polishing process, the single crystal was mounted on the lapping fixture (PELCO, 0.5 inch) using the thermoplastic wax (PELCO Quickstick 80C) at 80 °C and cooled to temperature to form a strong bond. The polishing experiment was conducted with the ECOMET III polisher (Buehler). The single crystal was first lapped with 600 grit silicon carbide paper, followed by coarse polishing with 1 µm aluminium oxide film and finally fine polishing with 0.3 µm aluminium oxide film. To avoid the ground powder scratching the surface, anhydrous isopropyl alcohol was continuously flushed into the single crystal during the process. The applied force to the sample was about 5 N, and the spin speed of the polishing disc was around 150 r.p.m. The polishing time was around 3 minutes for each step. After being polished, the single crystal was removed from the fixture by reheating the wax at 80 °C and washed in anhydrous isopropyl alcohol and cyclohexane. The polished single crystal was further dried in the vacuum chamber at 60 °C before use.

Superoxide generation

The superoxide probe stock solution was prepared by dissolving 1 mg of dihydroethidium probe (ThermoFisher) in 1 ml of CB; sonication was used to facilitate the dissolution. Perovskite films deposited on glass substrates were submerged into 10 ml of 0.01 mg ml^{-1} probe solution prepared from the stock solution with CB dilution. The solution was exposed to a visible light source emitted from a xenon lamp with an approximate light intensity of ~1.5 mW cm^{-2}. To prevent UV damage, a 520 nm long-pass optical filter was used for iodine perovskite systems. PL spectra were recorded using an excitation wavelength of 520 nm and bandwidth of 10 on an Edinburgh Instruments LP-920 laser flash photolysis system equipped with a pulsed 450 W xenon arc lamp. The laser power was 2.4 mJ cm^{-2}. The superoxide yield measurements were repeated two times to check reproducibility.

Preparation of halide exchange samples

To reach a homogenized mixed halide state close to 50 wt% halide in the exchange study, we made both the bromide and iodide layers with similar thicknesses. To do so, 0.8 M $FA_{0.8}Cs_{0.15}Rb_{0.05}PbI_3$ or $MAPbI_3$ perovskite precursor solution was prepared using DMF/DMSO in a 4:1 v/v mixed solvent. The iodide perovskite precursors were coated on a preprepared SnO_2-coated glass. The coating recipe for each perovskite layer was identical to what has been described for SIMS samples. Bromide samples, however, were coated on glass coated with styrene ethylene butylene styrene (SEBS) block copolymer. SEBS is a flexible block copolymer film that is removed from the glass substrate after MHP deposition and is laminated (face down) onto the MHP-coated glass substrate. SEBS-coated glass substrates were prepared by coating a 300 mg ml^{-1} solution of SEBS dissolved in toluene on octadecyltrichlorosilane-treated glass substrates. The main role of octadecyltrichlorosilane in these substrates is to create a hydrophobic surface that makes it easy for the perovskite/SEBS layer to be separated from the glass substrate during the lamination process. SEBS thin films with over 10 µm thickness were spin-coated on glass at 1,000 r.p.m. and subsequently baked at 100 °C for 15 minutes. The SEBS/glass substrates then were exposed to UV–ozone for at

least 60 minutes; this step is crucial for achieving full coverage of the perovskite on SEBS. The bromide perovskite coating and annealing recipe was identical to what has been described for SIMS samples. To create the final laminated bromide/iodide perovskite samples, 2 µl of CB was carefully dispersed on the perovskite/glass substrate. In the next step, the perovskite/SEBS samples, face down, were brought in contact with the perovskite/glass samples. The resulting laminated samples were annealed for 30 seconds at 60 °C to remove the excess CB left on the interface between the two layers. The annealing of laminated samples was performed on a nitrogen-gas-connected Linkam heating stage.

ToF-SIMS measurements

ToF-SIMS experiments were performed using an ION TOF-SIMS V instrument (ION TOF) equipped with a bismuth liquid metal ion gun, a Cs^+ sputtering gun and an electron flood gun for charge compensation. A burst alignment imaging mode was used to provide high lateral resolution and chemical resolution simultaneously, where Bi_3^{++} was employed as the primary ion and Cs^+ was employed as the sputtering source. Typical measurement conditions were ~0.12 pA Bi_3^{++} at 25 keV into a 200 × 200 µm^2 area (~3.6 × 10^{11} ion cm^{-2}). To avoid the edge effect during the mass sputtering, a sputter area of 400 × 400 µm^2 was selected (quadruple the size of the analysed area, 200 × 200 µm^2). The sputter beam was Cs^+ at 12 nA at 3 keV. Detection of negative ions was appropriate because of the high secondary ion yields for iodide and bromide in these samples. A flood gun was applied to neutralize any charge accumulated on the sample. The non-interlaced mode of ToF-SIMS with a pause analysis time of 2 seconds, sputter time of 10 seconds and pause time of 0.5 second was used to carry out the depth profilometry measurements. Depending on the perovskite film thickness and the sputtering rate, the total sputter time of the first ~10–150 seconds was used to create the 1D SIMS profiles and maps. The negative ion spectra were calibrated using C^-, CH^-, C_2H^-, Br^- and/or I^- ions. Both bismuth and caesium ion columns were oriented at 45° with respect to the sample surface normal. The analysis chamber pressure was maintained below 5.0 × 10^{-9} mbar to avoid contamination of the surfaces being analysed. High lateral resolution 2D SIMS images were collected using a PHI nanoTOF II system in unbunched mode. Bi_3^{++} was employed as the primary ion with ~0.5 pA Bi_3^{++} at 30 keV. The bismuth ion column was orientated at 60° with respect to the sample surface. PHI nanoTOF II system in bunched mode was used for single-crystal depth profilometry with a 20 keV-10 nA gas cluster ion beam as the sputtering source to provide a high depth resolution and chemical resolution simultaneously.

The µPL measurements

The µPL spectra were acquired using a Horiba LabRAM HR Evolution microscope with 473 nm laser excitation (objective, 0.75 numerical aperture, Olympus, ×50, <1 mW laser power) and a 300 l mm^{-1} grating with a beam size of ~0.32 µm^2. All samples were measured in air. Spectra were averaged for 0.5 second duration. The spectra were collected at 10 µm (Fig. 2c–e) and 1 µm (Supplementary Fig. 13) intervals.

Optical microscope images

The optical microscope images were taken with a Nikon Eclipse LV100POL microscope in a reflection mode. A ×20 objective was used with the exposure time set for 5 ms.

PV device fabrication and materials

The solar cell devices were structured in a typical negative–intrinsic–positive (n–i–p) configuration of FTO/c-TiO_2/m-TiO_2/$MAPbI_3$/spiro-OMeTAD/Au. Briefly, FTO glass was first precleaned by sequential ultrasonication in a bath of acetone, distilled water and ethanol for 30 min. After drying in an oven overnight, the FTO glass pieces were treated by UV–ozone for 40 min. Then, a compact layer of TiO_2 (c-TiO_2) was deposited onto FTO by spin-coating of titanium(IV) isopropoxide solution at 2,000 r.p.m. for 35 s, followed by thermal annealing at 150 °C for 30 min in ambient atmosphere. A mesoporous layer of TiO_2 (m-TiO_2) was further deposited onto the c-TiO_2 layer by spin-coating the paste solution (18NR-T TiO_2 paste diluted in ethanol with a weight ratio of 1:6) at 6,000 r.p.m. for 35 s, followed by thermal annealing at 100 °C for 30 min. The substrate was then put into a furnace for annealing at 500 °C for 30 minutes to complete the electron transfer layers. After cooling, the substrates were further treated by UV–ozone for 40 min before casting the perovskite layers. For different perovskites, all the perovskites (regardless of different compositions) were spin-coated inside a glove box (with moisture and oxygen concentration of <0.1 ppm). Specifically, the $MAPbI_3$ perovskite was cast from a one-step processing using a non-ionic ink (1.0 M $MAPbI_3$ in mixed solvents of methylamine solution (33 wt% in absolute ethanol) and acetonitrile in a volume ratio of 1:1), at a spin rate of 4,000 r.p.m. for 35 s, followed by annealing at 100 °C for 10 min. The $FA_{0.85}Cs_{0.15}PbI_3$ perovskite was cast from a one-step processing using an ink (1.3 M $FA_{0.85}Cs_{0.15}PbI_3$ in DMF/DMSO mixed solvent with a volume ratio of 4:1), at a sequential spin rate of 1,000 r.p.m. (ramp, 500 r.p.m.) for 10 s and followed by 5,000 r.p.m. (ramp, 2,000 r.p.m.) for 30 s, with an anti-solvent treatment using 150–200 µl CB executed at the last 10 s of the spinning. This process was further followed by annealing at 150 °C for 15 min to complete the conversion. For mixed halide perovskite ($FA_{0.85}Cs_{0.15}Pb(I_{0.8}Br_{0.2})_3$), similar methods were used to cast the perovskite films, noting that halide composition was pre-engineered in the precursor inks and an anti-solvent treatment was also included. After depositing the perovskite layer, the hole transfer layer of spiro-OMeTAD was cast directly on top of the perovskite at a spin rate of 4,000 r.p.m. for 35 s, using a preprepared solution (48 mg spiro-OMeTAD in 1 ml of CB, with the addition of 38 µl 4-*tert*-butylpyridine and 26 µl lithium salt solution from the stock solution of 520 mg in 1 ml of acetonitrile). Finally, an 80 nm gold electrode was deposited on top of the spiro-OMeTAD layer through a thermal evaporation process, with an active area of 0.096 cm^2 controlled by a shadow mask. The maximum power point measurements were carried out on unencapsulated devices in ambient air, at room temperature and with a relative humidity below 30%. Solar cell devices were tested under one-sun illumination (air mass, 1.5) using a xenon solar simulator (Class AAA Solar Simulator, IEC/JIS/ASTM, 450 W xenon, 2 inch × 2 inch). The light intensity of the simulator was calibrated to 100 mW cm^{-2} using a standard reference Si reference solar cell (Calibrated Reference Cell, KG3 Window, certified by the National Renewable Energy Laboratory). The spectral mismatch factor was maintained in a narrow range from 0.99 to 1.0.

Reporting summary

Further information on research design is available in the Nature Portfolio Reporting Summary linked to this article.

Data availability

Source data are provided with this paper. All other datasets generated and/or analysed during the current study are available from the corresponding authors upon request.

Code availability

The code used for the conversion of a 2D SIMS image to a matrix and subsequent integration for 2D-to-1D conversion is available from the corresponding authors upon request.

Acknowledgements

M.G. and A.A. acknowledge helpful discussions with D. Irving at North Carolina State University (NCSU) in relation to the GB strength model. M.G., B.G. and A.A. acknowledge support from Office of Naval Research grant N00014-20-1-2573. C.-W.H. and J.M.A. acknowledge support from the National Science Foundation

Chemical Measurement and Imaging programme under grant no. CHE-1848278. A.A., L.T., G.B., K.D. and M.G. also acknowledge the support of NCSU and the Carbon Electronics cluster for start-up funding (to A.A.). K.W. acknowledges support from the US Department of Energy's Office of Energy Efficiency and Renewable Energy under the Solar Energy Technologies Office, award no. DE-EE0009364. S.P. acknowledges support through the US Department of Energy's Small Business Technology Transfer programme (Prime – NanoSonic Inc.), no. DE-SC0019844. NanoSonic Inc. is lead on a Small Business Innovation Research project ("prime" is commonly used for indicating "lead"). Penn State has received a subcontract on this project. SIMS measurements were performed at the Analytical Instrumentation Facility at NCSU, which is partially supported by the State of North Carolina and the National Science Foundation, and the Materials Characterization Lab at Pennsylvania State University. We acknowledge C. Zhou for providing support for SIMS measurements. M.G. and E.D.G. acknowledge financial support from the Penn State Institutes of Energy and the Environment and Office of Naval Research grant no. N00014-19-1-2453 for X-ray photoemission spectroscopy and SIMS experiments. We acknowledge the support of B. Hengstebeck for SIMS and X-ray photoemission spectroscopy measurements at Pennsylvania State University and S. Koohfar for supporting the analysis of X-ray photoemission spectroscopy results. We also acknowledge F. Castellano for providing a PL facility for superoxide measurements. This report was prepared as an account of work sponsored by an agency of the United States Government. Neither the United States Government nor any agency thereof, nor any of their employees, makes any warranty, express or implied, or assumes any legal liability or responsibility for the accuracy, completeness, or usefulness of any information, apparatus, product, or process disclosed, or represents that its use would not infringe privately owned rights. Reference herein to any specific commercial product, process, or service by trade name, trademark, manufacturer, or otherwise does not necessarily constitute or imply its endorsement, recommendation, or favoring by the United States Government or any agency thereof. The views and opinions of authors expressed herein do not necessarily state or reflect those of the United States Government or any agency thereof. Abridged legal disclaimer: The views expressed herein do not necessarily represent the views of the US Department of Energy or the United States Government.

Author contributions

A.A. and M.G. conceived the scientific framework and designed all experiments. M.G. designed and executed experimental protocols, coordinated the experimental work, performed SIMS and halide exchange measurements and analysed SIMS results. M.G., B.G., G.B., B.M.L. and L.T. prepared the MHP samples used for different measurements. B.M.L. performed additional SIMS measurements. B.G. and K.D. performed the UV–visible absorbance measurements and degradation studies. T.W. prepared the perovskite single crystals and carried out the single-crystal mechanical polishing. M.C., B.G. and K.D. performed the superoxide measurements. K.D. performed the X-ray diffraction measurements. K.W. prepared PV devices and PV stability tests, and performed time-resolved PL measurements with the supervision of S.P.; M.G. prepared the X-ray photoemission spectroscopy samples and the samples used for SIMS using the PHI nanoTOF instrument, with the supervision of E.D.G.; and C.-W.H. and J.M.A. performed the μPL measurements and analysed the data.

Competing interests

The authors declare no competing interests.

Additional information

Supplementary information The online version contains supplementary material available at https://doi.org/10.1038/s41563-023-01488-2.

Correspondence and requests for materials should be addressed to Masoud Ghasemi or Aram Amassian.

Peer review information *Nature Materials* thanks Juan-Pablo Correa-Baena and the other, anonymous, reviewer(s) for their contribution to the peer review of this work.

nature research

Corresponding author(s): Aram Amassian, and Masoud Ghasemi

Solar Cells Reporting Summary

Nature Research wishes to improve the reproducibility of the work that we publish. This form is intended for publication with all accepted papers reporting the characterization of photovoltaic devices and provides structure for consistency and transparency in reporting. Some list items might not apply to an individual manuscript, but all fields must be completed for clarity.

For further information on Nature Research policies, including our data availability policy, see Authors & Referees.

Experimental design

Please check: are the following details reported in the manuscript?

1. Dimensions

Area of the tested solar cells	☒ Yes ☐ No	Area of the tested solar cells is provided in Methods section.
Method used to determine the device area	☒ Yes ☐ No	Calibrated Nikon visible light microscope is used to determine the device areas.

2. Current-voltage characterization

Current density-voltage (J-V) plots in both forward and backward direction	☒ Yes ☐ No	The forward and reverse scans with different delay times can be fund in supporting information.
Voltage scan conditions *For instance: scan direction, speed, dwell times*	☒ Yes ☐ No	Voltage scan conditions are provided in Methods section.
Test environment *For instance: characterization temperature, in air or in glove box*	☒ Yes ☐ No	Ambient air with below 30% relative humidity level
Protocol for preconditioning of the device before its characterization	☐ Yes ☒ No	No preconditioning of the devices were used in our study.
Stability of the J-V characteristic *Verified with time evolution of the maximum power point or with the photocurrent at maximum power point; see ref. 7 for details.*	☒ Yes ☐ No	MPPT is provided in the manuscript, Fig. S21 in SI

3. Hysteresis or any other unusual behaviour

Description of the unusual behaviour observed during the characterization	☐ Yes ☒ No	Hysteresis as a common characteristic of perovskite solar cells is also observed in this work. The hysteresis indexes calculated for different voltage delay time/sweep rates are presented in supporting information.
Related experimental data	☐ Yes ☒ No	We did not observe any unusual behavior in our PVs.

4. Efficiency

External quantum efficiency (EQE) or incident photons to current efficiency (IPCE)	☐ Yes ☒ No	EQE data is not included as EQE is not relevant to the diffusion physics discussion presented in our work.
A comparison between the integrated response under the standard reference spectrum and the response measure under the simulator	☐ Yes ☒ No	These measurements have not been performed as they are not relevant to this study.
For tandem solar cells, the bias illumination and bias voltage used for each subcell	☐ Yes ☒ No	We did not report any tandem devices in this study.

5. Calibration

Light source and reference cell or sensor used for the characterization	☒ Yes ☐ No	The information regarding the light source and reference cell is provided in Methods section.
Confirmation that the reference cell was calibrated and certified	☒ Yes ☐ No	This information is provided in Methods section.

Calculation of spectral mismatch between the reference cell and the devices under test	☒ Yes ☐ No	This information is provided in Methods section.

6. Mask/aperture

Size of the mask/aperture used during testing	☒ Yes ☐ No	The mask size during testing is provided in Methods section.
Variation of the measured short-circuit current density with the mask/aperture area	☐ Yes ☒ No	These measurements have not been performed as we did not aim to develop new devices or claim record-efficiency.

7. Performance certification

Identity of the independent certification laboratory that confirmed the photovoltaic performance	☐ Yes ☒ No	The photovoltaic performance of our PV devices has not been confirmed from independent certification laboratories, as we did not aim to claim record-efficiency.
A copy of any certificate(s) *Provide in Supplementary Information*	☐ Yes ☒ No	N/A

8. Statistics

Number of solar cells tested	☒ Yes ☐ No	At least ten devices have been tested for each system.
Statistical analysis of the device performance	☒ Yes ☐ No	We have included the average and standard deviation of power conversion efficiency in Table S3-S5.

9. Long-term stability analysis

Type of analysis, bias conditions and environmental conditions *For instance: illumination type, temperature, atmosphere humidity, encapsulation method, preconditioning temperature*	☒ Yes ☐ No	The information regarding to the type of the stability measurement and environmental conditions is provided in the Methods section.